N84 27271

SCANNING WIND-VECTOR SCATTEROMETERS WITH TWO PENCIL BEAMS

T. Kirimoto and R.K. Moore
Remote Sensing Laboratory
University of Kansas Center for Research, Inc.
Lawrence, Kansas 66045-2969, U.S.A.

Abstract

A scanning pencil-beam scatterometer for ocean windvector determination has potential advantages over the fan-beam systems used and proposed heretofore. The pencil beam permits use of lower transmitter power, and at the same time allows concurrent use of the reflector by a radiometer to correct for atmospheric attenuation and other radiometers for other purposes. The use of dual beams based on the same scanning reflector permits four looks at each cell on the surface, thereby improving accuracy and allowing alias removal.

This paper describes simulation results for a spaceborne dual-beam scanning scatterometer with a 1-watt radiated power at an orbital altitude of 900 km. Two novel algorithms for removing the aliases in the windvector are described, in addition to an adaptation of the conventional maximum-likelihood algorithm. The new algorithms are more effective at alias removal than the conventional one. Measurement errors for the wind speed, assuming perfect alias removal, were found to be less than 10%.

1.0 INTRODUCTION

Plans for wind-vector measurement with spaceborne radar scatterometers often call for measurements with a radiometer on the same spacecraft. Although many of these measurements may be independent of the scatterometer, at least some of them should be used to correct errors in the measured backscatter due to atmospheric attenuation. In fact, a radiometer should always be used in conjunction with a scatterometer for this purpose.

A major problem with this correction occurs when the radiometer and scatterometer have different scan patterns and the radiometer has a larger footprint than the scatterometer [Moore, et al., 1983], The problem exists because storm cells are often small compared with the size of a single radiometer footprint, so combining several radiometer measurements to correct a scatterometer measurement for a cell overlapping several radiometer cells results in significant errors in the "correction". The instrument configuration discussed here is intended to overcome this problem.

This arrangement calls for both instruments to have the same scan pattern and for the radiometer to have a footprint coincident with that of the scatterometer and, to the extent possible, a footprint of the same or smaller size. This is achieved by using the same scanning pencil-beam antenna for both scatterometer and radiometer. In addition, a second beam achieved by using an offset feed in the same antenna allows the scatterometer to have four rather than two azimuth angles (relative to the wind direction) for viewing each scatterometer cell.

The basic configuration is shown in Figure 1. Two circles at different distances from the suborbital track are shown, along with a line parallel to the track but displaced from it. The outer circle is the locus of scan positions for the radiometer and for scatterometer beam no.1, and the inner circle is the locus for scatterometer beam no. 2. The intersections of these circles with the

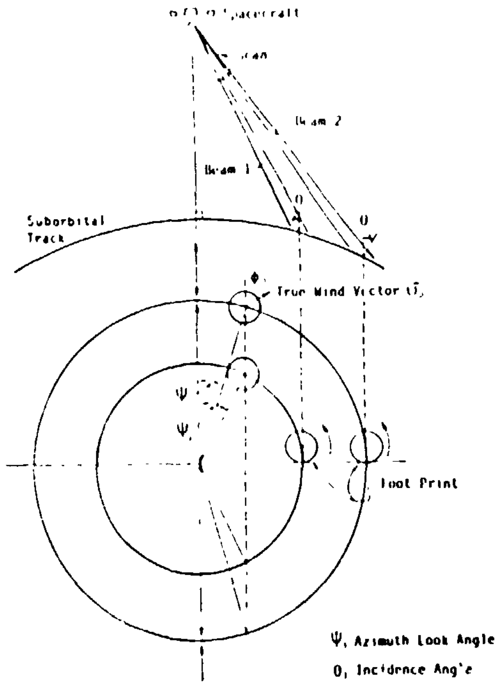

Fig. 1: Basic Configuration of Scanning Scatterometer

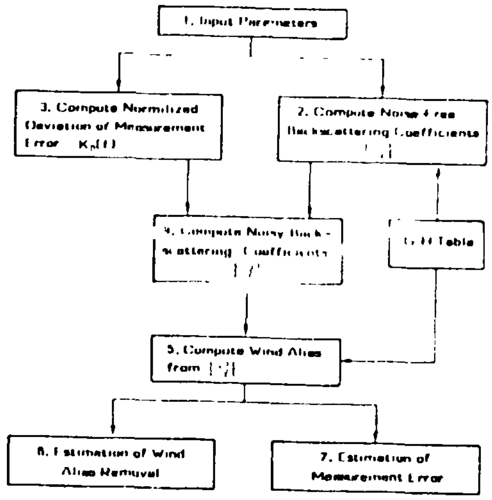

Fig. 2: Flow Chart for Simulation

displaced track line show the four different angles that are used by the scatterometer to view each cell on the surface. Use of only two look directions results in up to four "aliases" of the wind direction [Wurtele, et al., 1982] Use of additional beams can reduce this alias problem and allow determination of the correct wind direction much of the time without use of collateral data or pattern recognition [Shanmugan, et al., 1982] This paper presents simulations that illustrate how well the four-beam system solves the alias problem.

Advantages of this system include:

(1) Only one antenna is needed for both radiometer and scatterometer.

(2) Use of the relatively large aperture required for the radiometer allows the scatterometer power to be quite low (1 watt in these simulations).

(3) Since all scatterometer measurements are at only two fixed angles of incidence, errors in modeling the incidence-angle variation of the scattering coefficient do not exist, and the data processing for the scatterometer need not have algorithms to handle incidence-angle variations.

The primary disadvantage of this system is that the look directions for the different cells are neither orthogonal (as on SEASAT) nor constant. On the other hand, the effect of the rotation of the earth on the SEASAT observations was to make the orthogonal beams on the spacecraft more difficult to handle than they would have been if they had been oriented relative to the ground track rather than relative to the orbit plane. Hence the complexity in the computations associated with non-orthogonal beams is at least partly cancelled by the complexity associated with correcting for earth-rotation effects in the orthogonal-beam system. For some angular combinations with the scanning beam the accuracy is less than with orthogonal looks, but these may be avoided at some sacrifice in swath width.

Here we treat two subjects associated with the scanning-beam system:

algorithm development for determining wind vectors with the scanning four-beam scatterometer and measurement errors with such a system. The treatment is accomplished using Monte Carlo simulations. All simulations assume an effective transmitter average power of 1 watt at a spacecraft altitude of 900 km. Other parameters used are listed in Table 1. The algorithms used include a modification of the maximum-likelihood (or SOS) algorithm used for SEASAT [Jones, et al., 1982] and two simple pattern-recognition schemes based on comparison of results from nearby cells. The averages of norms between the true wind vectors and the simulated ones are computed to illustrate the errors.

2.0 SIMULATION METHOD

The major steps in the simulation of the scanning scatterometers are shown in Figure 2.

Step 1: Input of System Parameters: This step inputs all parameters that are needed in the following computation. The list of the parameters is shown in Table 1.

Step 2: Compute Noise-Free Backscattering Coefficients $\{\sigma_\ell^0\}$: This step computes a set of noise-free backscattering coefficients in equation (1).

$$\tilde{\sigma}_\ell^0\ (\text{dB}) = 10[G(\phi_0 - \psi_\ell - 180^0, \theta_\ell, \varepsilon_\ell) + H(\phi_0 - \psi_\ell - 180^0, \theta_\ell, \varepsilon_\ell)\log_{10}|\vec{U}_0|] \qquad (1)$$

where:

$\vec{U}_0$ = true wind vector
= $(|\vec{U}_0|\cos\phi_0, |\vec{U}_0|\sin\phi_0)$
ϕ_0 = true wind direction relative to suborbital track (see Figure 1)
ψ_ℓ = look angle relative to suborbital track (see Figure 1)
ℓ = notation to distinguish looks
θ_ℓ = incidence angle
ε_ℓ = polarization (HH or VV)
$G(\cdot), H(\cdot)$ = G-H Table [Schroeder, et al., 1982] describing the scattering model function

TABLE 1
PARAMETERS OF SIMULATION

Transmit Power (W)	1.0
Noise Temperature (°K)	273.0
System Loss (dB)	4.0
Noise Figure (dB)	4.0
Beamwidth-H (deg)	1.0
Beamwidth-V (deg)	1.0
Radiation Efficiency	0.8
Fraction of time to pass footprint k_I	0.1
Signal and Noise Integration Time Ratio k_N	10.0
Wavelength (MM)	22.0
Satellite Height (km)	900.0
Slant Range (km)	1127.6

ORIGINAL PAGE IS
OF POOR QUALITY

Step 3: Compute Normalized Standard Deviation of Measurement Error $K_p(\ell)$ Due to Noise. This step computes the normalized standard deviation $K_p(\ell)$ of measurement error [Grantham, et al.,] as

$$K_p^{\ 2}(\ell) = \frac{(1 + SNR^{-1})^2}{B_c T_I} + \frac{SNR^{-2}}{B_c T_I k_N} \tag{2}$$

where:

SNR = signal-to-noise power ratio
B_c = receiver bandwidth
T_I = signal integration time
k_N = noise-to-signal integration time ratio
ℓ = notation to distinguish looks.

Note that only the receiver noise is taken account of in these simulations, although the measurements might also be noisy because of sampling variability.

Step 4: Compute Noisy Backscattering Coefficients $\{\sigma^0_\ell\}$. This step computes the set of noisy backscattering coefficients $\{\sigma^0_\ell\}$ in equation (3). It is assumed that $\{\sigma^0_\ell\}$ are distributed log-normally.

$$\ln \sigma^0_\ell = \ln \tilde{\sigma}^0_\ell + \Delta\sigma^0_\ell \tag{3}$$

where:

$\Delta\sigma^0_\ell$ = Gaussian random variable with 0 mean and $K_p(\ell)$ deviation.
p = notation to distinguish looks.

Step 5: Compute Wind Alias from $\{\sigma^0_\ell\}$. The maximum-likelihood method is applied as the algorithm for computation of the wind alias from $\{\sigma^0_\ell\}$. Thus, the wind vectors $\vec{U}(=(|\vec{U}|\cos\phi, |\vec{U}|\sin\phi))$ at which the probability density function (PDF) of equation (4) have local maxima are computed [Jones, et al., 1982]

$$PDF(\vec{U}|\{\sigma^{ai}\}) = \frac{\exp\{-\sum_{\ell=1}^{4} (\ln\sigma^0_\ell - f(\vec{U},\ell))^2/2K_p^{\ 2}(\ell)\}}{\int dU \exp\{-\sum_{\ell=1}^{4} (\ln\sigma^0_\ell - f(\vec{U},\ell))^2/2K_p^{\ 2}(\ell)\}} \tag{4}$$

where:

$$f(\vec{U},\ell) = (\ln 10)[G(\phi-\psi_\ell - 180^0, \theta_\ell, \varepsilon_\ell) + H(\phi-\psi_\ell - 180^0, \theta_\ell, \varepsilon_\ell)]\cdot\log_{10}|U| \tag{5}$$

The procedures from Step 1 to Step 5 are iterated for several true wind vectors $\vec{U}_0$, ground points, incidence angles and two polarizations, because these parameters seriously influence wind alias and wind measurement error. Other parameters are fixed at suitable values for spaceborne systems. Wind-alias removal and measurement error are estimated in Steps 6 and 7.

3.0 WIND-ALIAS REMOVAL

The PDF of equation (4) usually results in two or four local maxima of the wind direction, resulting in wind aliases. The local probability maximum for a wrong wind vector often has a larger value than the local maximum of the correct wind vector. Hence, it is important to remove wind aliases by other means.

Examples of the simulation results are shown in Figures 4-13. Parameters of the simulation are shown in these figures and in Table 1. In these figures "ground-track" shows the direction of spacecraft motion and "AZ.Ang." shows forward azimuth look angles of each beam. (The reference axis is the ground-track). Aft azimuth look angles of each beam are given by subtracting forward look angles from 180°. The angle between the vector and "ground-track" shows the wind direction and the magnitude of the vector shows the wind speed.

Note that the type of "box" used for simulating the pattern recognition techniques is not completely realistic because it is based on the angles used for the simulations. The horizontal (j) dimension on the "chicken tracks" corresponds with along-track spacings for the satellite. The vertical (i) dimension on the "chicken tracks" corresponds to across-track spacings for the beam, but these dimensions are based on the angles selected for simulation rather than on uniform spacings. Figure 3 illustrates the dimensions of these boxes for different central angles chosen. A more realistic simulation would involve square boxes, but would mean repeating the simulations for these angles.

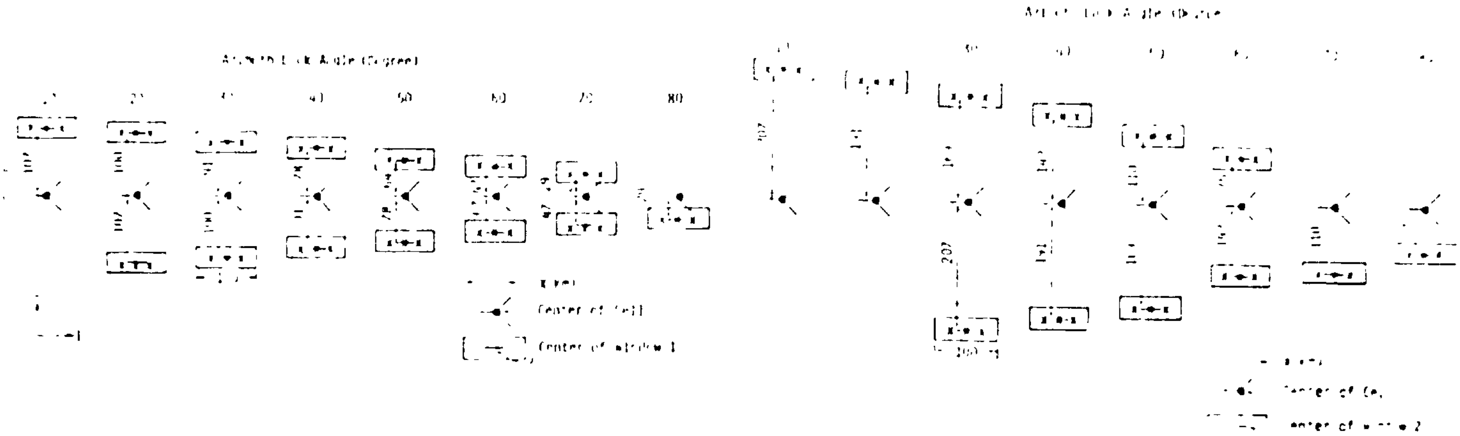

Fig. 3: Ground Spacings of Cells vs Azimuth Angle. (a) Outer Cells for Window 1; (b) Outer Cells for Window 2

The 4-vector plots ("sea chickens") shown in Figure 4a were prepared for each case studied, but only one example is presented here. These show the wind alias vectors, and -----X shows any wind alias whose normalized probability P(K), is over 0.1, where

$$P(K) = \frac{PDF(K)}{\sum_{K=1}^{K_n} PDF(K)} \tag{6}$$

where:

PDF = probability density function in equation (4).

K = notation to distinguish alias.

K_n = number of aliases.

The "Alias Removal" code shows the wind vectors which are selected by one of the following alias removal algorithms.

(1) <u>Algorithm 1 - (Maximum Probability)</u>

$$\vec{U}(I,J,K_c) \underset{K=K_c}{\leftarrow} \underset{K}{\mathrm{Max}}[P(I,J,K)] \tag{7}$$

In this algorithm, the alias that has maximum normalized probability is selected as the correct wind vector. Where:

$\vec{U}(I,J,K)$ = wind alias,

I,J = notation to distinguish ground point (see Figures 3(a) and (b)),

K = notation to distinguish alias,

$P(I,J,K)$ = normalized probability of wind alias.

Figure 4b shows an example of the wind vectors obtained by selecting the alias in Figure 4a using Algorithm 1 for 4 m/sec winds with vertical polarization for the forward beam pointed in the upwind direction. Since the results with Algorithm 1 are generally inferior to those with the other algorithms, the results obtained with this algorithm are not repeated for the other examples shown.

(2) Algorithm 2 - (Pattern Recognition - 1)

$$\vec{U}(I,J,K_c) \leftarrow \min_{K=K_c} \left[E_{ij}\left[\min_{k}\left\{|\vec{U}(i,j,k) - \vec{U}(I,J,K)|/|\vec{U}(I,J,K)|\right\}\right]\right] \tag{8}$$

In this algorithm, the wind alias which is satisfied with equation (8) is selected as the correct wind vector. There $E[\cdot]$ is the average over i and j and the ranges of i and j are as follows:

$$\text{(i)}\quad I-1 \leq i \leq I+1, \quad j = J-1, \quad J = J+1 \qquad \text{-Window 1} \tag{9}$$

$$\text{(ii)}\quad I-1 \leq i \leq I+1, \quad j = J-2, \quad j = J+2 \qquad \text{-Window 2} \tag{10}$$

(See Figure 3)

Window 1 uses adjacent cells in the pattern-recognition scheme, whereas Window 2 uses both adjacent cells and the next cell away in the cross-track direction. Thus, Window 1 uses 9 cells for alias removal, whereas Window 2 uses 15 cells. This is particularly important for the large azimuth angles, where the geometry of the simulation indicated in Figure 3 causes adjacent cross-track cells to be very close together. Of course, the assumption of uniform wind fields is more important in using Window 2.

Window 1 is used in Figures 4c and 5a to illustrate the use of Algorithm 2 (Pattern Recognition - 1). The other examples shown are for Algorithm 3 (Pattern Recognition - 2), since it gives better results.

(3) Algorithm 3 - (Pattern Recognition - 2)

$$\vec{U}(I,J,K_c) \leftarrow \min_{K=K_c}\left[E_{K\,ij}\left[\min_{k}\left\{-\ln\{P(I,J,K)\cdot P(i,j,k)\}\cdot |\vec{U}(i,j,k) - \vec{U}(I,J,K)|/|\vec{U}(I,J,K)|\right\}\right]\right] \tag{11}$$

In this algorithm, the wind alias which is selected by equation (11) is presumed to be the correct wind vector. The range of i,j is given by equation (9) or (10). This weighted algorithm gives generally better results than Algorithm 2. Therefore it is used in all of the examples following the initial ones that are shown in Figures 4 and 5 to illustrate the improvement of Algorithm 3 over Algorithm 2. Window 2 is used in Figures 6b, 7b, 10 and 13, since it gives significant improvement when the forward beam is in the crosswind (90°) direction.

The simulation results show the following:

(1) Every algorithm is apt to select wrong wind vectors in the case of low wind speed. The error pattern of algorithm 1 seems to be random, but the error patterns of algorithm 2 and of algorithm 3 seem to be more consistent. Thus, algorithm 2 and algorithm 3 are apt to select wind vectors 180° from the correct direction. This error can easily be removed by examining the wind patterns.

(2) Algorithm 2 is apt to select opposite wind vectors even in the case of high wind speed.

(3) Window 2 improves the performance of Algorithm 2 and of Algorithm 3.

(4) Algorithm 3 with window 2 will select correct wind vectors almost perfectly.

Note that the low-wind-speed errors might be reduced by use of higher power than the 1 watt assumed. They would also be smaller if the satellite were at a lower altitude than 900 km.

4.0 MEASUREMENT ERROR OF WIND VECTOR

In this section, the measurement error of the wind vector (after alias removal) is investigated. It is presumed that the alias-removal algorithm works perfectly. Scanning scatterometers with one beam (two look angles) are also investigated here.

The simulation results are shown in Figures 14-16. Parameters of the simulation are shown in Table 1 and in these figures. In these figures the horizontal axes show the forward look angle of the inner beam. The vertical axes show measurement error MC

$$MC = \frac{\sqrt{E[|\vec{U}| - |\vec{U}_o|^2]}}{|\vec{U}_o|} \tag{12}$$

where:

$\vec{U}_o$ = true wind vector.

$\vec{U}$ = simulated wind vector.

Twenty-five noisy samples of wind vectors were simulated in look directions relative to the wind of 0°, 30°, 60° and 90°. Hence, one hundred samples are used in the average of equation (12). These figures show that vertical polarization, small incidence angle, and high wind speed reduce measurement error of scatterometers because they increase received power. Higher power at larger incidence angles might improve performance, but no such simulations were performed.

The averages of 2400 simultion samples as to three wind speeds (4.0 m/s, 12.0 m/s, 24 m/s), four wind directions (0°, 30°, 60°, 90°) and eight azimuth look angles (10°, 20°, 30°, 40°, 50°, 60°, 70°, 80°) are shown in Table 2. The rows of Table 2 show parameters (incidence angle and polarization) of the inner beam and the columns show parameters of the outer beam. Although a smaller incidence angle is better for scatterometers, scatterometers whose incidence angle is 50° for the outer beams were investigated because 50° is often used in radiometers, and because 50° gives a wider measurement swath. These figures and Table 2 obviously show the following:

(1) Two-beam (four-look) scatterometers are better than one-beam (two-look) scatterometers.

(2) Two-beam scatterometers give quite low measurement error over look angles from 20° to 80° off the surface track.

(3) The simulation results in the case of low wind speed are not good, but an increase (i.e., to two watts) in transm... power would resolve this problem easily.

TABLE 2

AVERAGE MEASUREMENT ERROR

1 \ 2		35 HH	35 VV	40 HH	40 VV	45 HH	45 VV	50 HH	50 VV
35	HH	.088		.060		.062		.068	
	VV		.064						
40	HH			.114			.058	.093	.058
	VV				.069				.044
45	HH					.161		.128	.090
	VV						.087		.056
50	HH							.255	
	VV								.098

DIAGONAL - SINGLE-BEAM SCATTEROMETER

5.0 CONCLUSIONS

Wind alias removal and measurement error of wind vector in scanning two-beam scatterometers were estimated using computer simulation. In the estimation of wind alias removal, two novel algorithms using pattern recognition technique were introduced and simulation results showed these algorithms are more powerful than the conventional maximum-likelihood algorithm. Note that these algorithms would not be powerful in scatterometers with fixed fan beams like SEASAT SASS. In the estimation of measurement error of wind vector, simulation results showed the scanning scatterometers give low enough measurement error over an arc from 20° to the side of the spacecraft track to 80° to the side to be practical. The average of measurement error was under 10.0%.

Only receiver noise was taken account of as the primary factor of noise in this simulation. Other noise sources should be taken account of in future studies. Additional noise would increase K_p. However, it is possible to reduce K_p by increasing transmit power. Only 1-watt transmit power was used in this simulation. More detailed studies would make certain that the scanning scatterometers are very powerful spaceborne wind-vector-measurement systems.

REFERENCES

Grantham, W.L., et al., "An Operational Satellite Scatterometer for Wind Vector Measurement Over the Ocean," NASA Tech Memo TMX-72672.

Jones, W.L., et al., "The SEASAT-A Satellite Scatterometer: The Geophysical Evaluation of Remotely Sensed Wind Vector Over the Ocean," J. Geophys. Res., vol. 87, April 1982, pp. 3297-3317.

Moore, R.K., A.H. Chaudhry and I.J. Birrer, "Errors in Scatterometer-Radiometer Wind Measurement Due to Rain," IEEE J. Ocean Engr., vol. OE-8, no. 1, January 1983, pp. 37-49.

Schroeder, L.C., et al., "The Relationship Between Wind Vector and Normalized Radar Cross-Section Used to Derive SEASAT-A Satellite Scatterometer Winds," J. Geophys. Res., vol. 87, April 1982, pp. 3318-3336.

Shanmugan, K.S., V. Narayanan and J. Stiles, "NOSS-SCAT Wind Direction Alias Removal," Remote Sensing Laboratory Technical Report 515-1, University of Kansas Center for Research, Inc., Lawrence, Kansas, January 1982.

Wurtele, M.G., et al., "Wind Direction Alias Removal Studies of SEASAT Scatterometer-Driven Wind," J. Geophys. Res., vol. 87, April 1982, pp. 3365-3377.

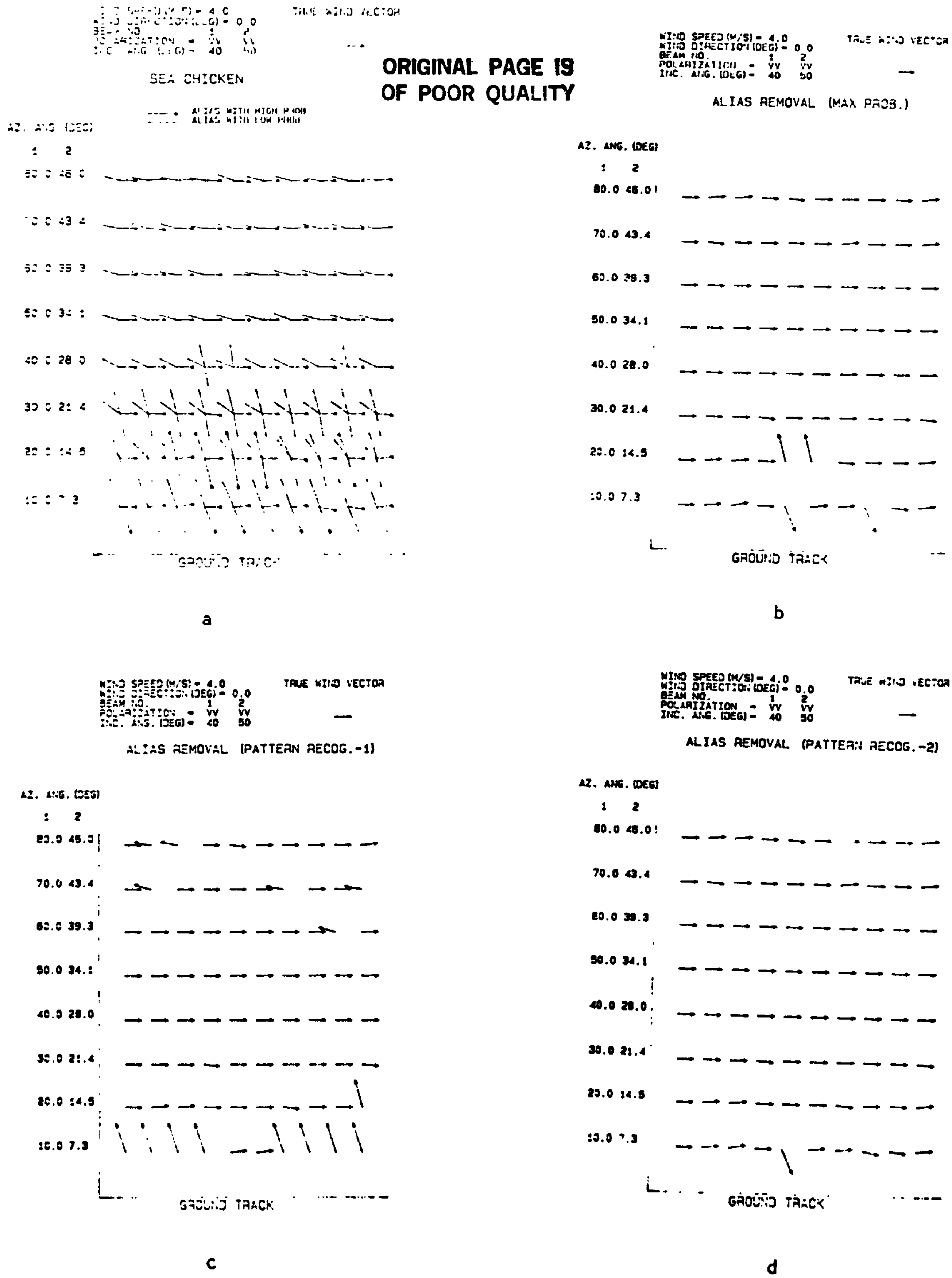

Figure 4: Examples for Different Stages in Alias Removal. Wind Speed 4 m/sec. Look Angle 0° (Upwind for Forward Beam). Vertical polarization. (a) Result of basic algorithm, showing aliases; (b) Aliases with maximum probability on basic algorithm; (c) Aliases selected by algorithm 2; (d) Aliases selected by algorithm 3.

ORIGINAL PAGE IS
OF POOR QUALITY

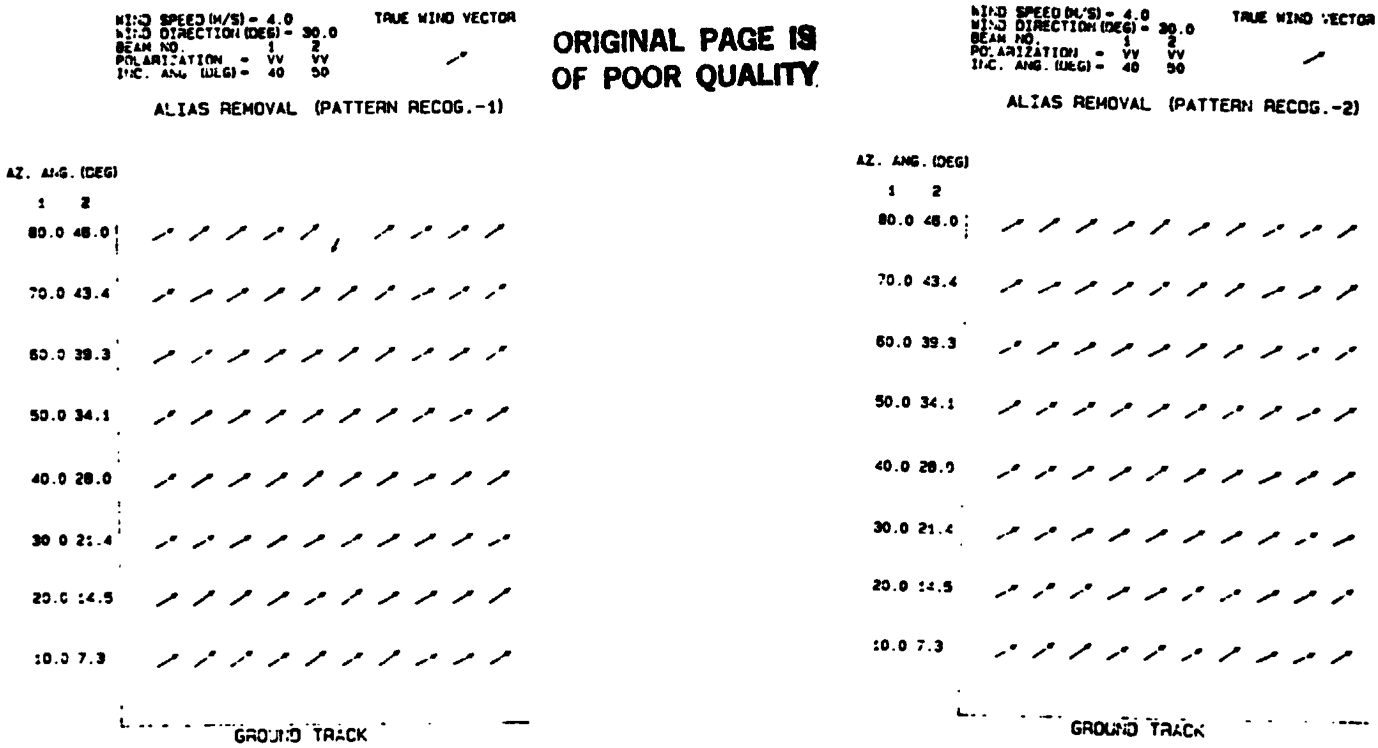

Figure 5: Examples for Algorithms 2 and 3. Wind Speed 4 m/sec. Look Angle 30°. Vertical Polarization. (a) Algorithm 2; (b) Algorithm 3.

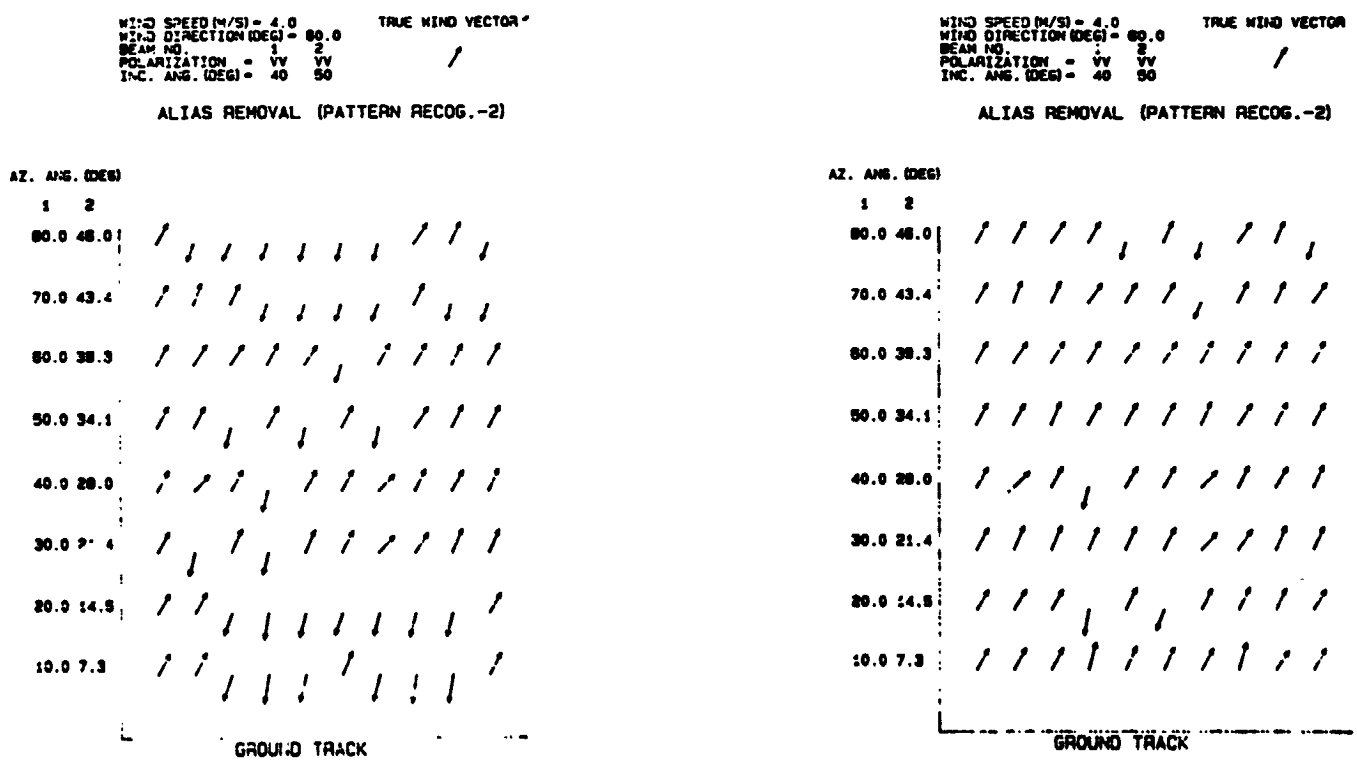

Figure 6: Examples for Algorithm 3, Windows 1 and 2. Wind Speed 4 m/sec. Look Angle 60°. Vertical Polarization. (a) Window 1; (b) Window 2.

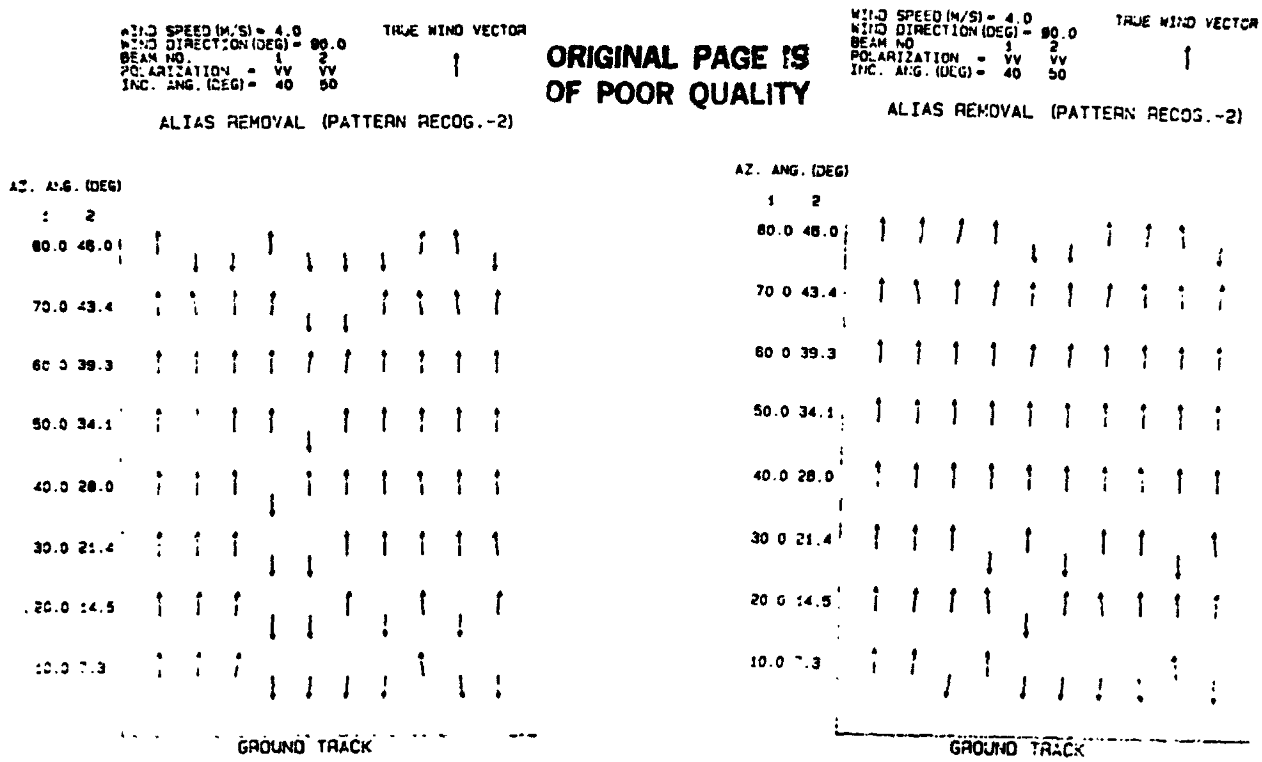

Figure 7: Examples for Algorithm 3, Windows 1 and 2. Wind Speed 4 m/sec. Look Angle 90°. Vertical Polarization. This look angle is always the worst case. (a) Window 1; (b) Window 2.

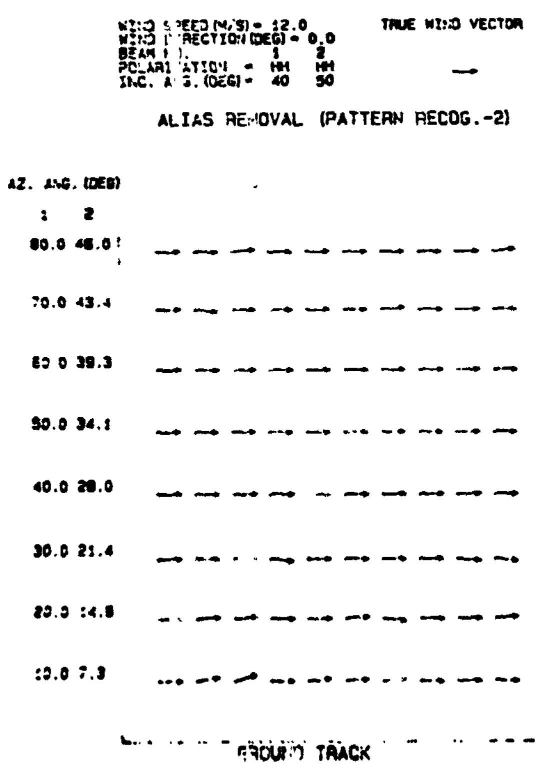

Figure 8: Example for Algorithm 3, Window 1. Wind Speed 12 m/s. Look Angle 0°. Horizontal Polarization.

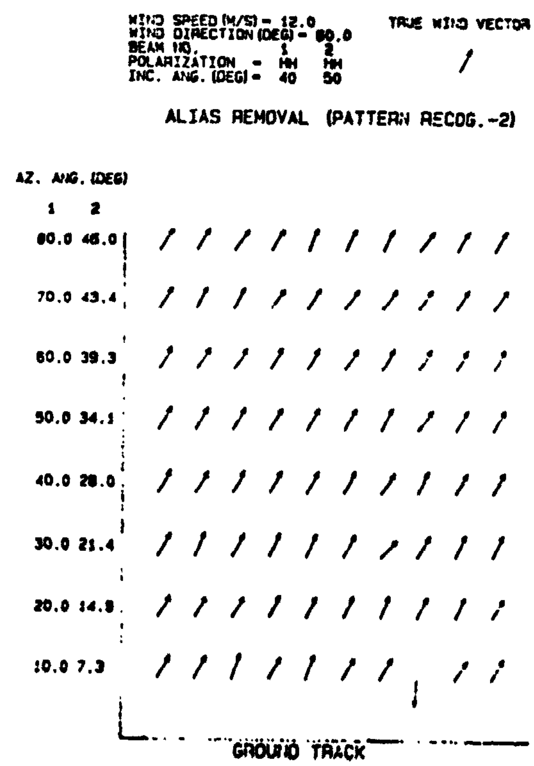

Figure 9: Example for Algorithm 3 Window 1. Wind Speed 12 m/s. Look Angle 60° Horizontal Polarization

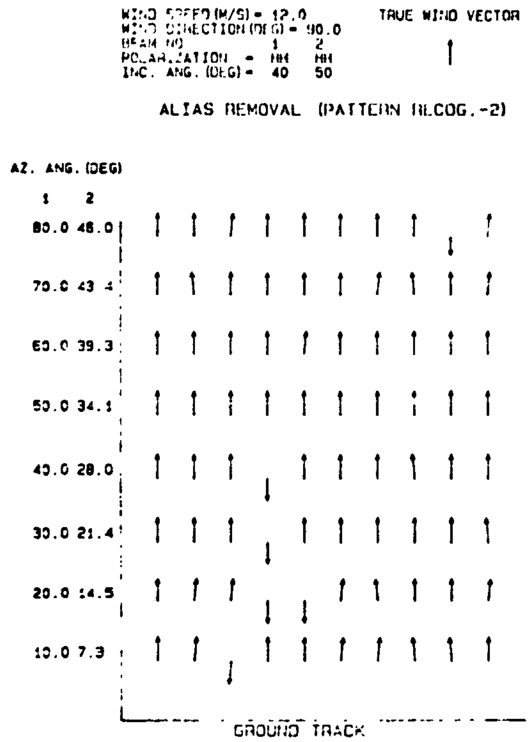

Figure 10: Example for Algorithm 3, Window 2. Wind Speed 12 m/s. Look Angle 90°. Horizontal Polarization.

ORIGINAL PAGE IS OF POOR QUALITY

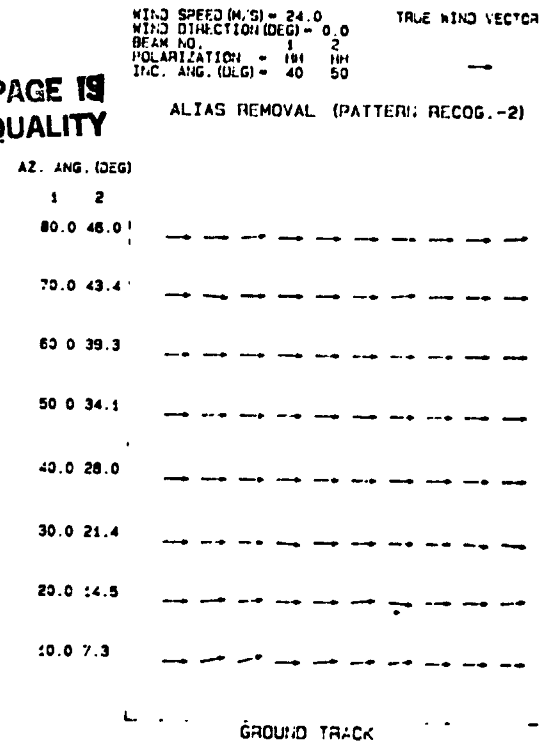

Figure 11: Example for Algorithm 3, Window 1. Wind Speed 24 m/s. Look Angle 0°. Horizontal Polarization.

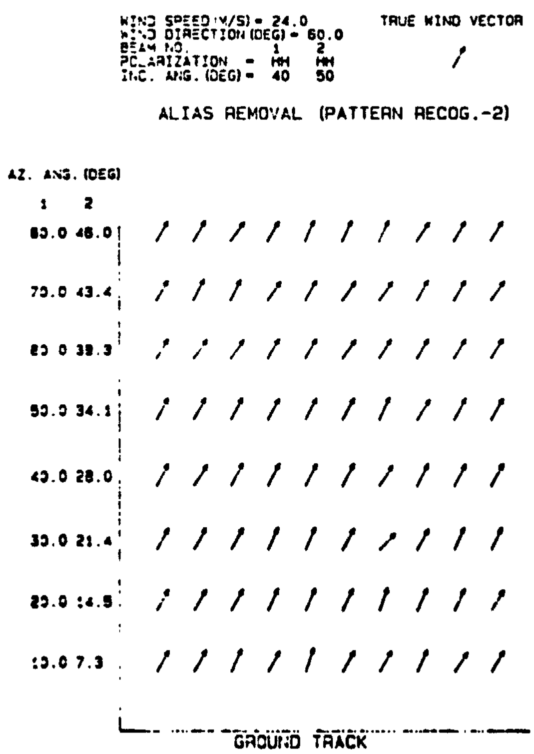

Figure 12: Example for Algorithm 3, Window 1. Wind Speed 24 m/s. Look Angle 60°. Horizontal Polarization.

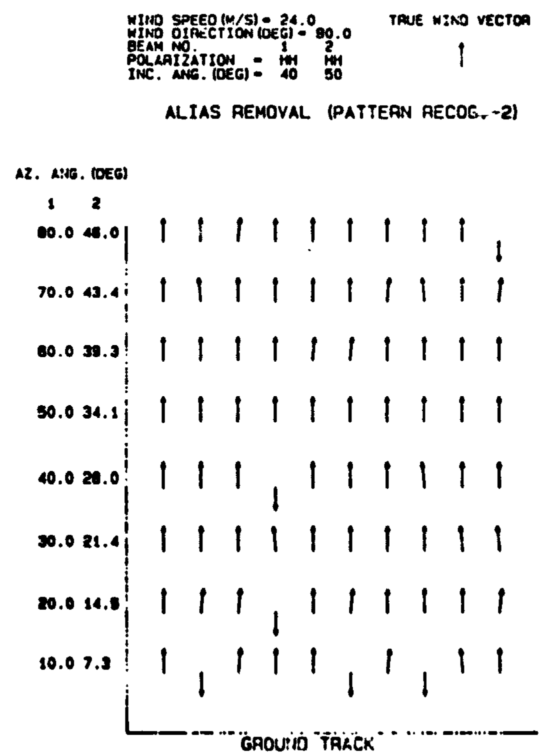

Figure 13: Example for Algorithm 3, Window 2. Wind Speed 24 m/s. Look Angle 90°. Horizontal Polarization.

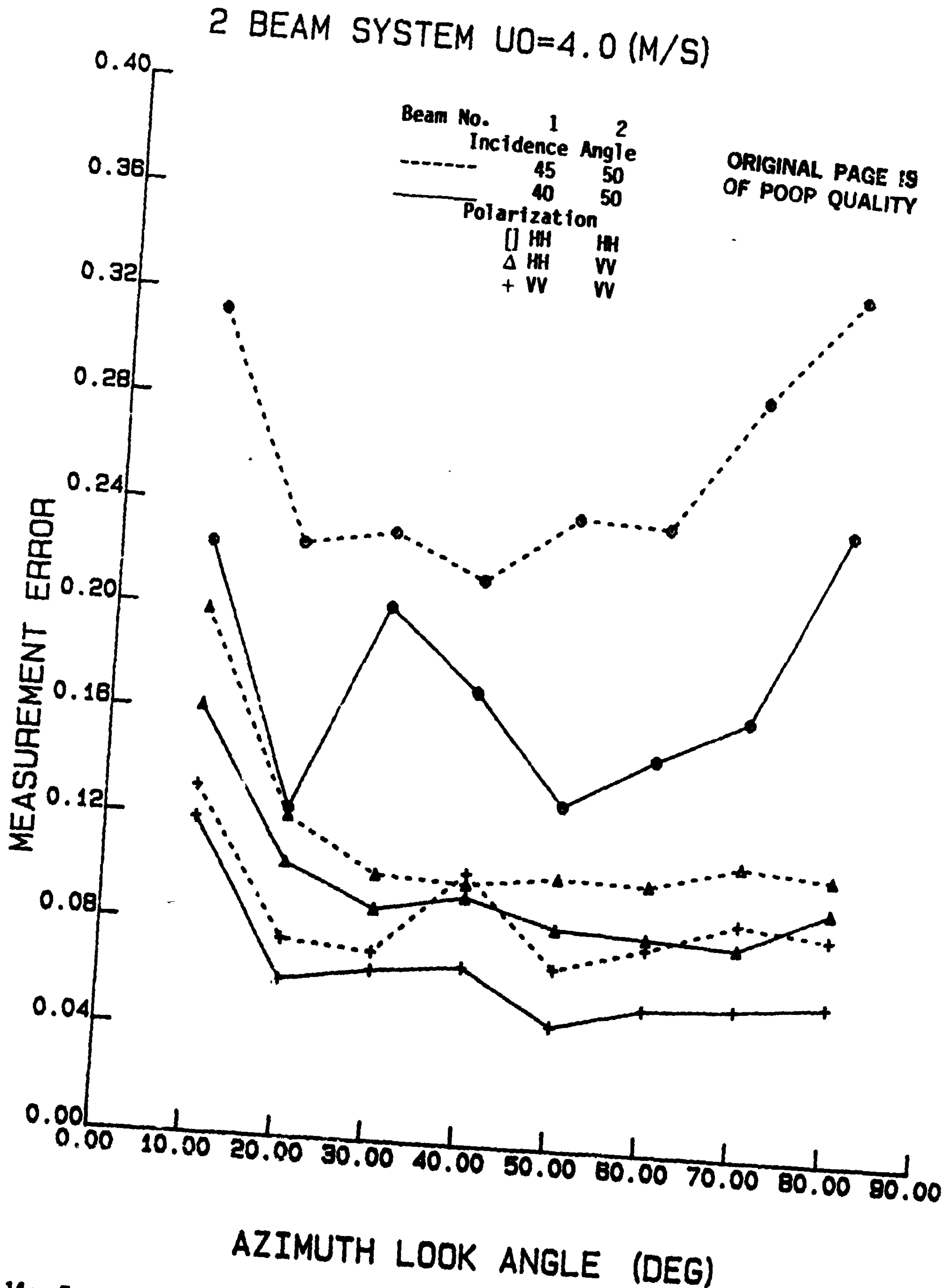

Figure 14: Errors for Wind Speed of 4 m/sec vs Azimuth Angle with Beam Incidence Angles and Polarizations as Parameters.

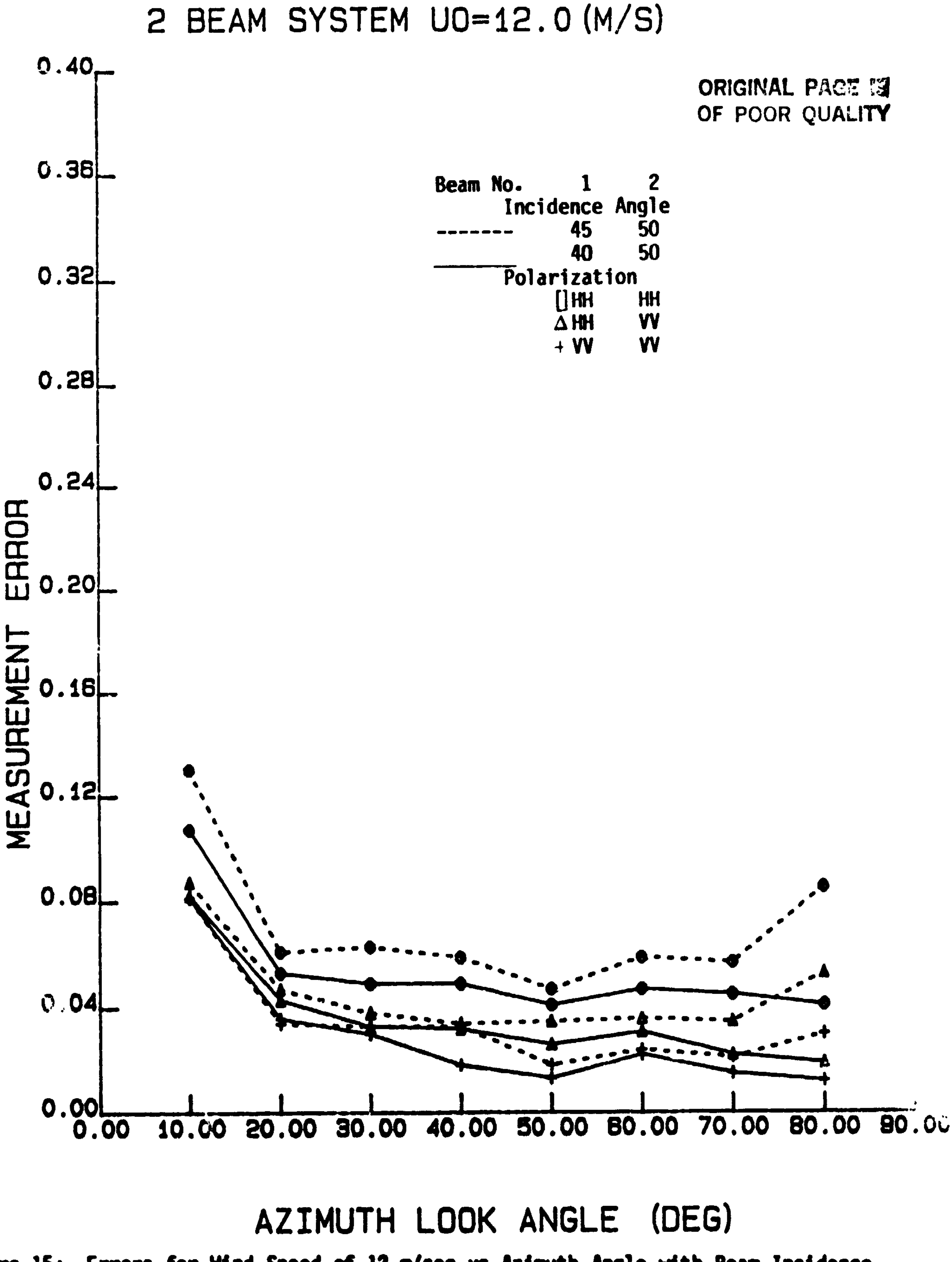

Figure 15: Errors for Wind Speed of 12 m/sec vs Azimuth Angle with Beam Incidence Angles and Polarizations as Parameters.

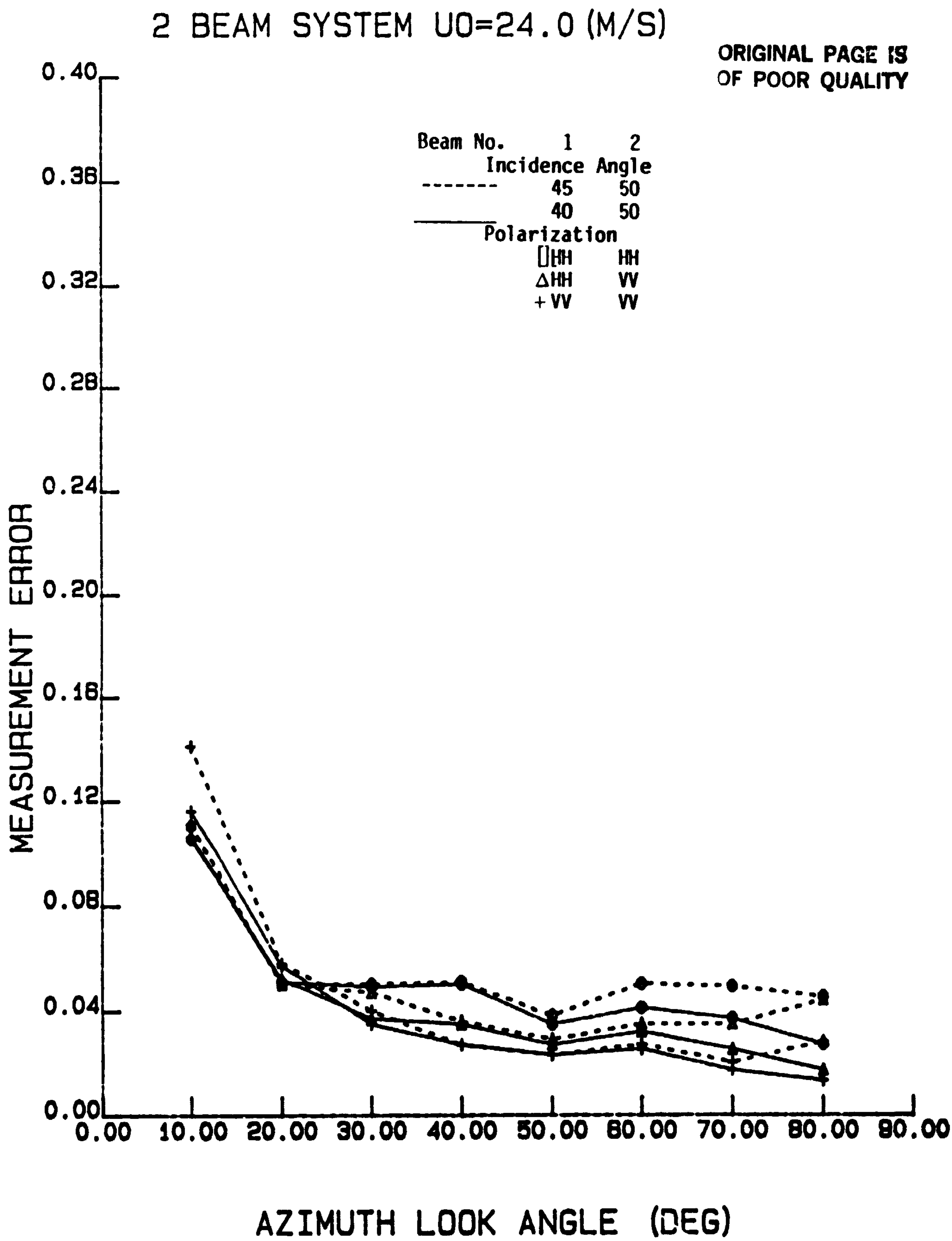

ORIGINAL PAGE IS
OF POOR QUALITY

Figure 16: Errors for Wind Speed of 24 m/sec vs Azimuth Angle with Beam Incidence Angles and Polarizations as Parameters.